Automatically Locate Tropical Cyclone Centers Using Top Cloud Motion Data Derived From Geostationary Satellite Images

Gang Zheng, *Senior Member, IEEE*, Jianguo Liu, *Member, IEEE*, Jingsong Yang, and Xiaofeng Li, *Senior Member, IEEE*

Abstract—This article presents a novel technique for automatically locating tropical cyclone (TC) centers based on top cloud motions in consecutive geostationary satellite images. The high imaging rate and spatial resolution images of the Gaofen-4 geostationary satellite enable us to derive pixel-wise top cloud motion data of TCs, and from the data, TC spiral centers can be accurately determined based on an entirely different principle from those based on static image features. First, a physical motion field decomposition is proposed to eliminate scene shift and TC migration in the motion data without requiring any auxiliary geolocation data. This decomposition does not generate the artifacts that appear in the results of the previously published motion field decomposition. Then, an algorithm of a motion direction-based index embedded in a pyramid searching structure is fully designed to automatically and effectively locate the TC centers. The test shows that the TC concentric motions are more clearly revealed after the proposed motion field decomposition and the located centers are in good agreement with the cloud pattern centers in a visual sense and also with the best track data sets of four meteorological agencies.

Index Terms—Geostationary satellite, motion field decomposition, tropical cyclone (TC), typhoon eye.

I. INTRODUCTION

TROPICAL cyclones (TCs) are intense warm-cored cyclonic vortices, developed from low-pressure systems over the tropical oceans and driven by complex air-sea interaction [1]. Recent trend analyses based on both archive data and future projections consistently suggest an increase of the mean intensity of global TCs over coming decades [2]–[6], although there could be a decrease in TC frequency [7], [8].

G. Zheng and J. Yang are with the State Key Laboratory of Satellite Ocean Environment Dynamics, Second Institute of Oceanography, Ministry of Natural Resources, Hangzhou 310012, China (e-mail: gang_zheng@outlook.com).

J. Liu is with the Department of Earth Science and Engineering, Imperial College London, London SW7 2AZ, U.K., and also with the State Key Laboratory of Satellite Ocean Environment Dynamics, Second Institute of Oceanography, Ministry of Natural Resources, Hangzhou 310012, China.

X. Li is with the National Environmental Satellite, Data, and Information Service, NOAA, College Park, MD 20740 USA.

Research on TCs has, therefore, become more important and urgent than ever before.

Accurate determination of TC centers is important to forecast track and intensity of TCs, in order to take timing prevention measures to reduce damages of hazardous TCs [9]–[14]. In this article, we present a method for automatically tracking of TC centers reliably and accurately using high-resolution (50 m) panchromatic images acquired by the Gaofen-4 (GF-4) satellite in very high imaging rate.

Various spaceborne optical sensors have been widely used to monitor and study TCs because of their large coverage, improving spatial resolution, and high imaging rate. Visual-near infrared (VNIR) sensors receive radiation reflected from top clouds of TCs have a typical resolution of hundreds of meters to few kilometers. Manual TC-center determination based on image features, such as tracing the movement of spiral rainbands or overlaying spiral templates on remote sensing images for the best match [9], is commonly used but the process is subjective and time-consuming. Therefore, the relevant research efforts have been focused on objectivity and automation, as reviewed below.

Spiral structure feature is diagnostic in images of TCs and provides a cue to find TC centers. In an early spiral feature-based TC center determination algorithm [15], a skeleton of the spiral cloud is extracted, and the points on the skeleton are then fitted using logarithmic spiral curve model, and the rotation center of the model with the best fit is determined as the TC center. The model was then applied to weather radar images, where the pixels of a whole image were taken instead of those on the skeleton, and a genetic algorithm was used to optimize the parameters (including the rotation center) of the model [16]. A similar automatic algorithm using IR satellite images was also given in [17]. The model was further improved by using the logarithmic spiral band model instead of the logarithmic spiral curve model to improve the robustness, and the parameters were optimized by a chaos immune evolutionary algorithm [18]. In addition to the spiral structure feature, the near elliptic structure feature (surrounding the cyclone central dense overcast region) in thermal IR images could also be used to locate TC centers based on the ellipse curve model to fit the closed brightness-temperature contours near the cyclone center [19]. A brightness-temperature gradient-based algorithm was proposed for IR images [20]. In the algorithm, the brightness-temperature gradient field is

calculated from a TC IR image first, using a Sobel operator. Then, a line aligning with the gradient vector at each pixel is drawn across the whole image, and the number of lines passing through each location in the image are counted and stored in a matrix. The location corresponding to the largest matrix element is considered as the TC center. A similar algorithm was also given in [9], where the gradient field of brightness-temperature variance value in a moving window is used instead of the brightness-temperature gradient field. In the algorithm presented in [21], cloud candidate regions are segmented from an IR satellite image, using image binarization and morphology operators. Then, the region, including a TC, is recognized using a so-called weight slice method, and the centroid of the region is considered as the TC center.

Recently, the application of synthetic aperture radar (SAR) in TC observation has been a focus of researches [11], [13], [22]–[34]. By benefiting from high spatial resolution and cloud-penetrating capability of microwaves, SAR can clearly capture a TC eye at sea surface level even if the eye is completely covered by dense clouds [30]. Then, the centroids of the captured eyes can be used to locate the TC centers. In order to make SAR-derived TC centers objective, several studies were carried out to extract TC eyes from SAR images using various image-processing techniques, including wavelet analysis, morphology operators, and binarization and watershed segmentation [11], [23], [26], [28]–[30]. For the case of a TC partially covered by a SAR image, salient regions were extracted based on the gray-level standard-deviation and Gabor-feature maps, which mainly contain rain bands of the TC; and then, the pixels on the skeleton of the longest salient region were used to estimate the TC center, using an analytical model of storm-relative inflow angle and a particle swarm optimization algorithm [13].

Above reviewed studies on TC-center determination are based on static features of TCs in a single remote sensing image. Motion features of TCs revealed by consecutive images can be used to locate TC centers as well [35]. One of such algorithms is inspired by the property of a perfect logarithmic spiral vector field: the angle between an arbitrary vector in the field and the radial vector (relative to the field center) at the same position is constant [35]. If this angle is approximately compensated, the field will degrade into an approximate sink vector field, and the location that most vectors point to is considered as the center. This algorithm was applied to locate TC centers from vector fields derived from a sequence of radar intensity images of a 3-km constant altitude plan position indicator. The algorithm requires several parameters, including the angle, to be empirically estimated in advance, and can be improved by adaptive estimation [35]. Overall, compared with the static feature-based methods, motion feature-based TC-center estimation is less studied and yet to be further explored.

Winds at cloud level can be estimated from motions of cloud features in two consecutive VNIR cloud images and their imaging interval [36]. These wind data are usually called "atmospheric motion vectors (AMVs)" (sometimes also called "cloud motion vectors"), which provide valuable motion information and can be used for TC center determination.

However, most current AMV observations are derived from medium-size (typically from few to tens of kilometers cloud features [37], and so, can describe only the general airflow [38]. The studies in [38]–[40] show that high spatial and temporal resolution AMVs can better capture details of airflow dynamics that are characterized by small and rapidly-changing cloud features. TC cloud structures are typically fast-evolving due to deformation, evaporation, and vertical shear [41], [42], and cloud features are usually too short-lived to be tracked by routine imaging intervals of meteorological satellites (e.g., 30 min). The study in [43] demonstrates the significance and effectiveness of shorter imaging intervals (3–7.5 min) for improving the observation of rapidly changing features in TC cloud images. Obviously, improving AMV spatial and temporal resolution is essential to tracking cloud features in a TC system, especially in the high-speed zone of the eyewall [37], [41], [43], [44]. Since the 1960s, when cloud motion was manually identified and measured initially [45], various objective methods were developed to extract AMVs, such as block matching [36], [46]–[48], object feature matching [49]–[51], and optical flow algorithms [52]–[54].

In this article, pixel-wise AMVs were derived from pairs of TC images of GF-4, using the phase correlation (PC) image analysis system (PCIAS) [55]–[57]. As migration of a TC system and translation induced from possible sensor swing can distort centralized motion (rotation, converge, or radiation) of TC, a physical meaningful motion field decomposition is proposed in this article to eliminate the translation components and extract the centralized motion components from the initial AMV data. Finally, an algorithm of a motion direction-based index embedded in a pyramid searching structure is fully designed to automatically and effectively locate the TC centers. The whole proposed technique, comprising the motion field decomposition algorithm and the TC Center determination algorithm, is new and novel.

II. TOP CLOUD MOTION DATA AND MOTION FIELD DECOMPOSITION

A. GF-4 Satellite

GF-4 is the first Chinese high-resolution geostationary satellite launched on December 29, 2015. It stationaries at 35 786 km above the Equator at 105.6° E and carries a staring optical camera [58]. The camera has a panchromatic/NIR (PNIR) CCD array sensor and an intermediate infrared (IIR) HgCdTe array sensor, which share the same aperture but are separated by a color filter. The PNIR sensor has five spectral bands (0.45–0.90, 0.45–0.52, 0.52–0.60, 0.63–0.69, and 0.76–0.90 μm) and can acquire images of different bands successively through a rotary filter. The IIR has one band (3.5–4.1 μm). For the PNIR sensor, the focal length is 6600 mm, pixel size 9 μm, image size $10\,240 \times 10\,240$, nominal resolution 50 m, and field of view angle $0.8^\circ \times 0.8^\circ$, while for the IIR sensor these sensor parameters are 1350 mm, 15 μm, 1024×1024, 400 m, $0.6^\circ \times 0.6^\circ$, respectively. The first PNIR band is a panchromatic band with wider spectral range and higher signal-to-noise ratio (SNR) than the other PNIR bands, we used this band images in digital number for this article, which cover areas of about 512 km × 512 km.

The high spatial-temporal resolution of GF-4 images enables derivation of high-resolution AMVs, and thus, provide a good opportunity to explore TC-center determination based on its concentric motion characteristics. In a very recent case study of typhoon Nepartak-2016, GF-4 image derived AMVs of the TC eye area were used to refine the TC center [59]. This article is a further advance toward fully automatic locating TC centers in large regions covering the entire TC system and adjacent areas using high spatial–temporal resolution GF-4 images.

B. Top Cloud Motion Data

Consecutive images of several typhoons acquired at intervals of tens of seconds captured the motion of the top clouds of the typhoons nearly continuously. As thick clouds of a typhoon are typically opaque to VNIR sensors and of rich texture, it is possible to estimate the motion of typhoon top clouds at every pixel by image matching, and thus, to generate time series of the motion fields from these GF-4 images. This motion field is limited on the cloud-top altitudes of a typhoon.

An in-house software package, the PCIAS, has been used to derive typhoon AMVs [60]. PC is one of the most effective, accurate, and robust techniques for image disparity estimation at subpixel accuracy [61]–[65]. In principle, it is based on the well-known Fourier shift property: a linear translation between two resembling images in the spatial domain results in a phase shift in the frequency domain of their Fourier transforms (FT) [66]. Through aerial correlation between two overlapped images, the shift between them can be identified directly in the frequency domain at subpixel magnitude, based on the spatial textures formulated by all the image pixels involved in the comparison. This matching process can proceed pixel-by-pixel via scanning, using a correlation window to compare neighborhood patches of each pair of corresponding pixels in the two images [55]–[57], thus deriving disparity maps (ΔX, ΔY) of translation between every pair of corresponding pixels in the two images. As an aerial matching-based algorithm, PC has a low tolerance to the geometric distortion between the two images in matching. Fortunately, the consecutive GF-4 images are taken by the same camera in nearly identical geometric status, and therefore, best suited to the PC algorithm. Other algorithms based on feature points, such as scale-invariant feature transform [67] and speeded-up robust features [68], although can cope with considerable geometric distortion, are not robust for and often not capable of matching the features of continuous varying clouds because of the lacking of consistent corresponding feature points for matching.

We have processed GF-4 images of several typhoons, including Megi-2016, using the PCIAS to derive the motion field data of typhoon top clouds.

C. Motion Field Decomposition

As described in Section II-A, a top cloud motion field can be extracted from a pair of consecutive GF-4 images of a TC; this field includes both translation and concentric (rotation and radiation) motions of the TC during the time interval between the two images. The translation includes
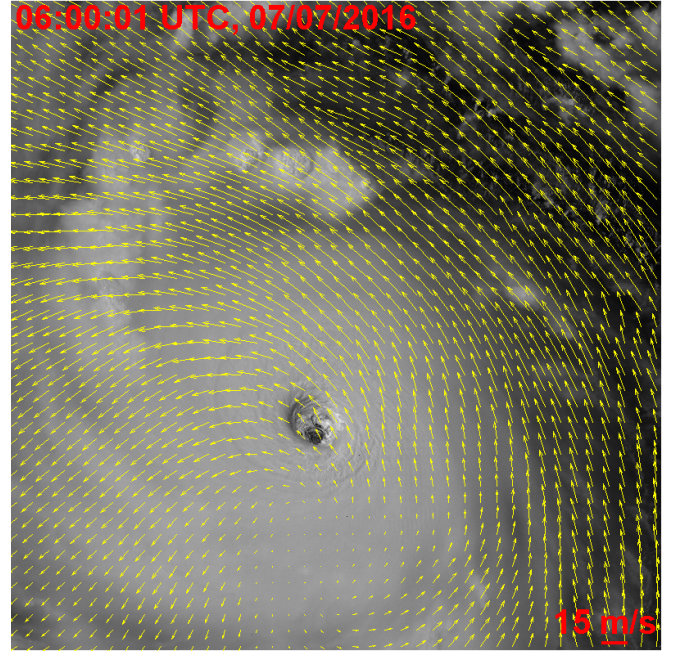

Fig. 1. Motion field generated by the PCIAS from a pair of GF-4 images of Typhoon Nepartak-2016 and denoted with yellow arrows.

not only the migration of the whole TC system but also the scene shift resulting from steering the camera to chase the TC system and the minor instability of the imaging platform. For instance, Fig. 1 presents a motion field generated by the PCIAS from a pair of GF-4 images of Typhoon Nepartak-2016. From the GF-4 image, we can see a clear eye in the cloud structure. However, the motion field of the pair does not show obvious concentric motion because of the co-existed translational motion. The translation component of the TC motion field needs to be removed to estimate the TC center accurately. In principle, the scene shift can be compensated using the auxiliary geolocation information, the four corner geo-coordinates of the two images, but an effective correction requires very high accuracy of these coordinates. If we can decompose the TC motion field into translation and concentric motion components, all the translational motions for whatever causes can all be removed. We, therefore, designed a motion field decomposition algorithm to remove the above mentioned translational components from the top cloud motion field without requiring any auxiliary geolocation information.

A 2-D motion vector field $\vec{V}$ inside a domain Ω can be decomposed as follows [69]:

$$\vec{V} = \vec{V}_\psi + \vec{V}_\chi + \vec{V}_0 \qquad (1)$$
$$\vec{V}_\psi = \hat{z} \times \nabla \psi \qquad (2)$$
$$\vec{V}_\chi = \nabla \chi \qquad (3)$$

where $\times$ and ∇ denote cross product and the Nabla operator, respectively. The symbols $\rightarrow$ and $\wedge$ denote vector and unit vector, respectively. $\hat{z}$ is the unit vector perpendicular to the plane of Ω inwards, and the scales Ψ and χ satisfy

$$\nabla^2 \psi = \hat{z} \cdot \nabla \times \vec{V} \qquad (4)$$
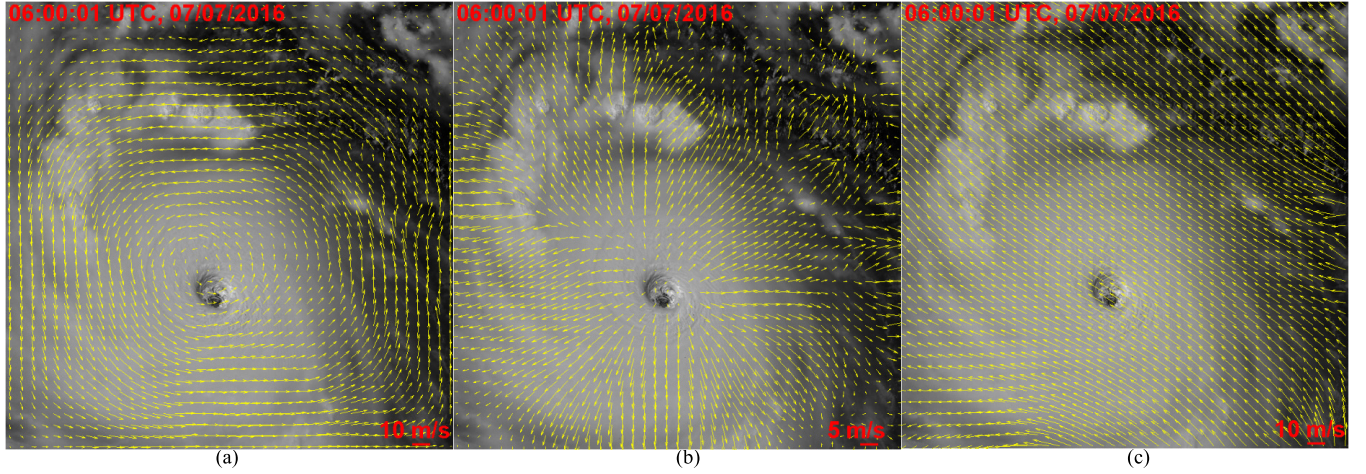$$\nabla^2 \chi = \nabla \cdot \vec{V} \qquad (5)$$

Fig. 2.   Motion field in Fig. 1 is decomposed using the previous method [69], and the motion components are denoted with yellow arrows. (a) Rotation component, (b) divergence component, and (c) harmonic component.

where · denotes dot product and ∇^2 is the Laplace operator. From (2)–(5), it can be proved that $\vec{V}_\psi$ has the same curl of $\vec{V}$, and it is divergence-free while $\vec{V}_\chi$, the same divergence of $\vec{V}$, and curl-free. Thus, the residual field $\vec{V}_0$ is free of both curl and divergence. Here $\vec{V}_\psi$, $\vec{V}_\chi$, and $\vec{V}_0$ are called the rotation, divergence, and harmonic components of $\vec{V}$, respectively. The decomposition based on the above definition is not unique, but with a physical constrain appropriately relevant to the problem, a unique decomposition can be resolved. The cloud motion field should be decomposed with such a physical constrain: within a limited domain Ω with open boundary, which means that there is no real physical interface between the limited domain and its surrounding free space.

In a commonly used three-component decomposition approach presented in [69], $\vec{V}_\psi$ and $\vec{V}_\chi$ are calculated using (2) and (3), where Ψ and χ are resolved from the Poisson equations of (4) and (5) with the Dirichlet boundary condition of imposing constant Ψ and χ on the boundary of Ω. However, the Dirichlet boundary condition is not truly representative for a limited domain with open boundary, and it induces artificial phenomena in $\vec{V}_\psi$ and $\vec{V}_\chi$. For instance, no matter whatever the distribution of $\vec{V}$ is, the $\vec{V}_\psi$ and $\vec{V}_\chi$ decomposed based on the Dirichlet boundary condition are always parallel and perpendicular to the boundary in the margin along the boundary, as illustrated in Fig. 2, which presents the results of decomposing the motion field in Fig. 1. This is because when imposing the Dirichlet boundary condition, the boundary becomes contour lines of Ψ and χ, and thus, the above artificial phenomena appear as implied by (2) and (3).

In this article, instead of solving (4) and (5) with the imposed boundary condition, we derived Ψ and χ in Ω using the Green function of Poisson equation in free space, and the final simplified formulas for calculating $\vec{V}_\psi$ and $\vec{V}_\chi$ at the center of the pixel (m, n) are

$$(\vec{V}_\psi)_{m,n} = \frac{h_x h_y}{8\pi} \hat{z} \times \sum_{m'=1}^{M} \sum_{n'=1}^{N} (\hat{z} \cdot \nabla \times \vec{V})_{m',n'} \vec{G}_{m-m',n-n'} \quad (6)$$

$$(\vec{V}_\chi)_{m,n} = \frac{h_x h_y}{8\pi} \sum_{m'=1}^{M} \sum_{n'=1}^{N} (\nabla \cdot \vec{V})_{m',n'} \vec{G}_{m-m',n-n'}. \quad (7)$$

The derivation of (6) and (7) is given in the Appendix. M and N are total numbers of rows and columns of an image, respectively, and h_x and h_y are the size of a pixel in column and row directions, respectively. $(\hat{z} \cdot \nabla \times \vec{V})_{m,n}$ and $(\nabla \cdot \vec{V})_{m,n}$ are values of $\hat{z} \cdot \nabla \times \vec{V}$ and $\nabla \cdot \vec{V}$ at the center of the pixel (m, n), respectively, and $\vec{G}_{m,n}$ is

$$\vec{G}_{m,n} = \begin{cases} 0 \\ \qquad m = 0 \text{ and } n = 0 \\ \int_{-1}^{1} \int_{-1}^{1} \frac{\xi h_x \hat{x}/2 + \eta h_y \hat{y}/2 - \vec{r}_{m,n}}{|\xi h_x \hat{x}/2 + \eta h_y \hat{y}/2 - \vec{r}_{m,n}|^2} d\xi d\eta \\ \qquad \text{else cases} \end{cases} \quad (8)$$

where

$$\vec{r}_{m,n} = \vec{r}_{1,1} + (n-1)h_x \hat{x} + (m-1)h_y \hat{y}. \quad (9)$$

$\hat{x}$ and $\hat{y}$ are unit vectors in column and row directions, respectively, and they satisfy the right-hand rule in relation to $\hat{z}$. $\vec{r}_{m,n}$ and $\vec{r}_{1,1}$ point to the centers of pixels (m, n) and $(1, 1)$. The integral in (8) can be conveniently calculated using Gaussian quadrature. The convolution in (6) and (7) can be effectively carried out using FT and inverse FT. Fig. 3 shows the results of the proposed decomposition. It can be seen that the artificial phenomena no longer appear in the rotation and divergence components. Moreover, while the rotation component obtained using the previous decomposition obviously does not center at the TC eye, as shown in Fig. 2(a), the rotation component obtained using the proposed decomposition does, as shown in Fig. 3(a). The harmonic component indicates that there is a large translation, which severely distorts the rotation and radial motions and makes them indistinctive in the original motion field shown in Fig. 1. With the harmonic component removed, the concentric motion is clearly revealed in the rotation and divergence components. For a clearer illustration, the eye and its surrounding area of Figs. 2 and 3 are zoomed in as Fig. 4 in which, the motion components decomposed by the previous
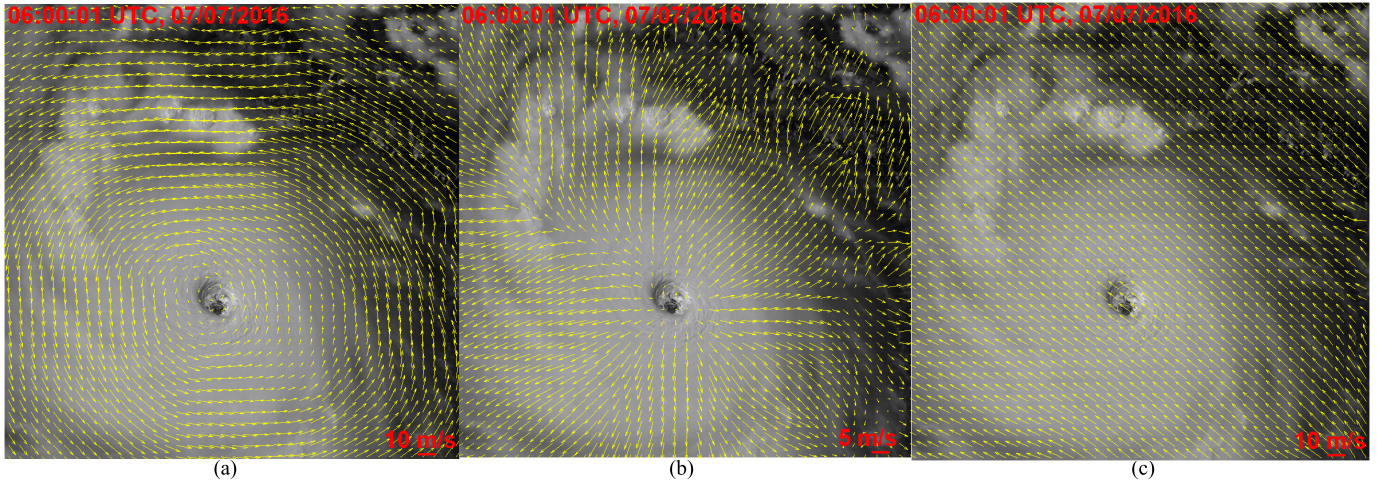
Fig. 3. Motion field in Fig. 1 is decomposed by the proposed method, and the motion components are denoted with yellow arrows. (a) Rotation component, (b) divergence component, and (c) harmonic component.
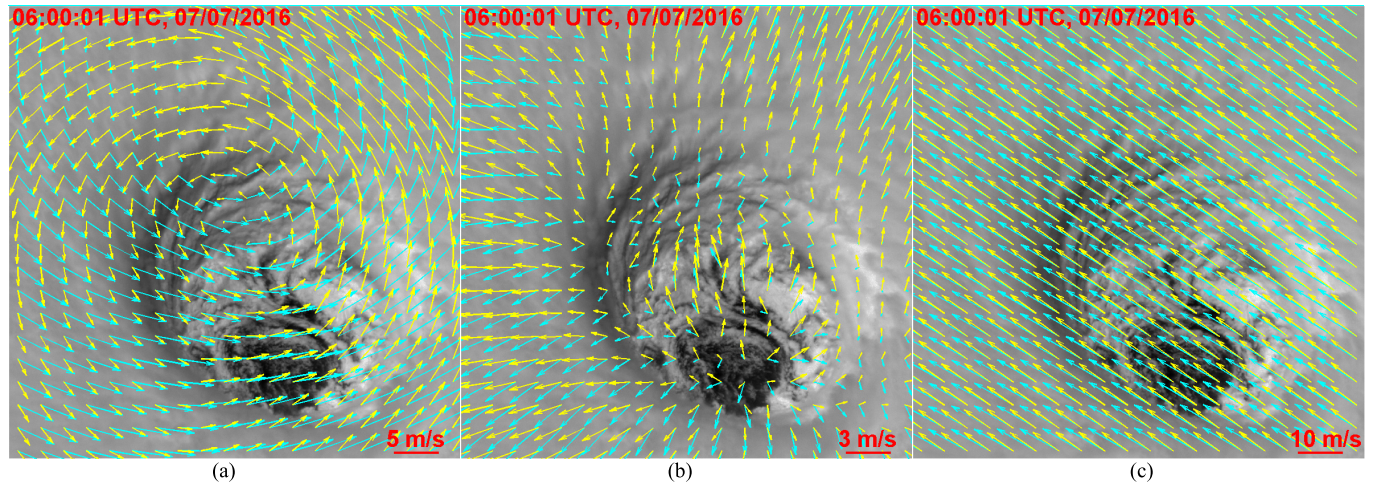

Fig. 4. Eye area of Fig. 1 and the motion components of Figs. 2 and 3 are zoomed in. The motion components decomposed by the previous method [69] and the proposed method are denoted with cyan arrows and yellow arrows, respectively. (a) Rotation component, (b) divergence component, and (c) harmonic component.

method and the proposed method are denoted with cyan and yellow arrows, respectively. Fig. 4(a) clearly demonstrates that the center of the rotation component derived using the previous method does not match the image feature of the typhoon eye, while that derived using the proposed method achieved a good matching. As indicated in Fig. 4(b), the corresponding divergence component of the previous method shows concentration inside a small area of the eye and radiation outside. Such motion in the opposite direction around a typhoon eye cannot be explained from the typhoon dynamics. In contrast, the divergence component of the proposed method shows consistent radiation in all directions from the eye as expected for a mature TC system. The harmonic components by the two methods are basically consistent with the minor discrepancy in Fig. 4(c).

III. TC Center Determination Algorithm

The center of a TC system in its motion field is a point where motion in all direction (rotation or radiation) converges

with the lowest motion speed, and it is, therefore, possible to locate the TC center automatically based on the motion direction in combination with the motion speed of the TC motion field data.

Considering that motion direction converging at the TC center is the most typical characteristic of the TC cloud motion field, a motion direction-based indicator is designed to search the center of concentric motion in the field. For a motion vector in any direction, we can represent its motion direction on a unit circle according to its compass angle as a unit direction vector. For a perfectly symmetric concentric motion (e.g., rotation and radiation), the direction vector at any location in the neighborhood of the motion center has its opposite counterpart at the symmetric location. Thus, the mean of the direction vectors should be equal to zero. The greater the magnitude of the mean of the direction vectors (MMDV), the less concentric the motion. Therefore, we can use the MMDV as an indicator to search the center of concentric motion by its minimal. The MMDV is the distance between the mean position of the terminal points of direction vectors in the unit circle and
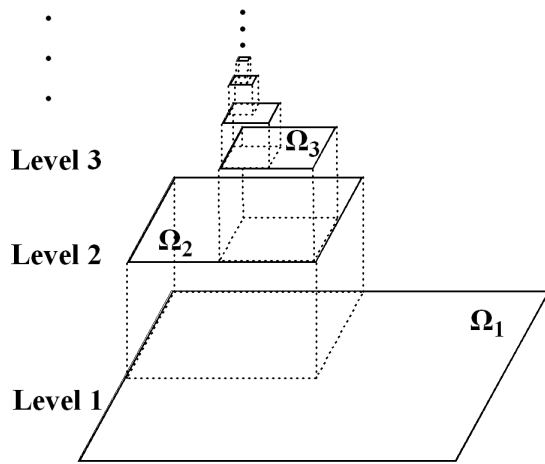
Fig. 5. Diagram of the pyramid, where the search areas at its levels (1, 2, 3, …) are represented by solid boxes (Ω_1, Ω_2, Ω_3, ...). The initial box is the entire image, and the box size at a specific level is a quarter of the box size at the level below.

the circle center. We could also consider using the standard deviation (SD) of direction vectors (SDDV) as an indicator, and the largest SDDV may lead to the center of concentric motion. As a measure of vector directions deviating from the mean of the direction vectors, the largest SDDV can only be reached when MMDV is equal to zero. However, fairly large SDDV may be produced at nonzero MMDV, and for this scenario, SDDV becomes a less robust indicator for motion center. In the experiments so far, both indicators performed equally competently to locate the TC centers. We choose to use the MMDV for its better mathematical rationale and simplicity in the calculation.

The above MMDV-derived TC center determination utilizes motion direction of motion fields regardless of motion speed. We can further tune a TC center located based on the MMDV to the location with the minimum motion speed in its neighborhood as the speed-adjusted TC center. In experiments, it is not surprising to find that the speed-adjusted TC centers are usually very close or overlap with the MMDV-derived centers as the TC rotation center is often of the lowest speed.

We then designed a pyramid searching scheme to locate the TC centers automatically based on the above indicators (MMDV and the lowest motion speed around the MMDV-derived TC center). By starting from the total image area as the initial search area, the scheme is to reduce the searching area step by step leading to the actual TC center based on a recursion procedure.

1) Calculate and search for the smallest-MMDV among candidate areas at the current level of the pyramid as the possible area, including the TC center.
2) Choose the candidate area with the smallest-MMDV as the search area for the upper level and partition it into smaller candidate areas.
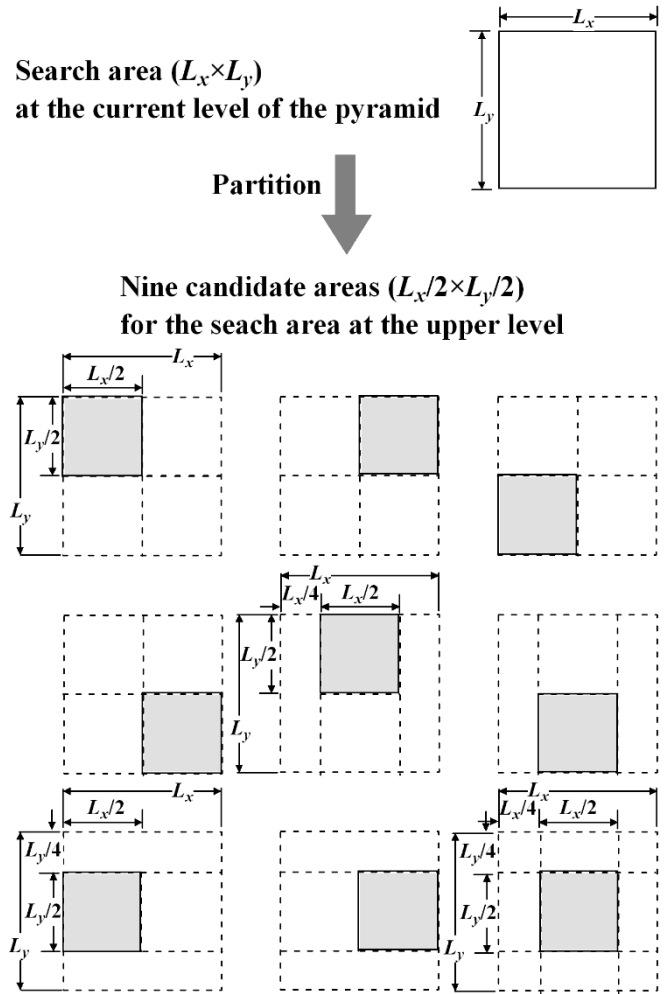3) Repeat 1)–2) till the TC center is located at the pixel level.

Fig. 6. Search area partition rule used in this article. The search area (big solid box at the top of the figure) at the current level of the pyramid is partitioned into nine smaller areas (shaded boxes) with its one-fourth size as candidates for the search area at the upper level. The nine candidate areas are the top-left, top-right, bottom-left, bottom-right, top-middle, bottom-middle, middle-left, middle-right, and center parts of the search area at the current level. Some of these partitions partially overlap.

Fig. 5 illustrates the scheme in a pyramidal diagram in which the search area at each level is represented by a solid box. The center of the final search area at the top of the pyramid is determined as the MMDV-derived TC center. Further, as an optional step, the MMDV-derived TC center can be tuned by searching the location with the minimum motion speed in its neighborhood as the speed-adjusted TC center.

The above conceptually described pyramid searching scheme based on the MMDV for locating a TC center is mathematically implemented in five steps to be described below. Here we denote the search area and the jth candidate area at level i of the pyramid as Ω_i and $\Omega_{i,j}$, respectively. The initial search area (Ω_1) is the entire search area. The candidate area set at level i is denoted as $\{\Omega_{i,j}\}$.

Step 1: Convert the motion directions of the motion vectors at all the pixels in the motion field as direction vectors on a unit compass circle.

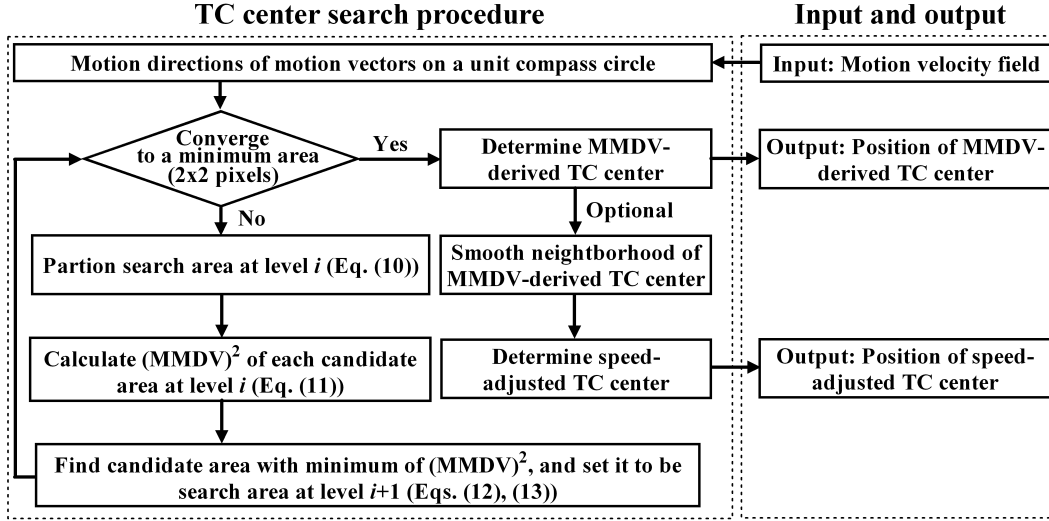**TC center search procedure** | **Input and output**

Fig. 7.   Flowchart of the proposed TC center determination algorithm.

Step 2: Partition the search area Ω_i at level i into a set of smaller areas ($\{\Omega_{i,j}\}$) as candidates for the search area at level $i+1$ according to a partitioning rule designed for fair search. This step is denoted as follows:

$$\{\Omega_{i,j}\} = S(\Omega_i) \tag{10}$$

where S denotes the partition operation. The partition rule used in this article is illustrated in Fig. 6. The top big solid box represents the current search area at a particular level in the pyramid. Nine candidate areas are defined in this search area, as shown by the small shaded boxes. These candidates are subareas in the top-left, top-right, bottom-left, bottom-right, top-middle, bottom-middle, middle-left, middle-right, and center part of the current search area with its one-fourth size. Some of these candidate areas are designed to partially overlap to avoid the concerned TC center area being truncated by the partition. For rectangular images, the partition at the first level can be easily modified accordingly, but the chosen search areas after the first partition will always be square.

Step 3: Calculate the square of MMDV of each candidate area at level i. The square of MMDV of the jth candidate area ($\Omega_{i,j}$) at level i is

$$f(\Omega_{i,j}) = |\underset{p \in \Omega_{i,j}}{\text{mean}}(\hat{d}_p)|^2 \tag{11}$$

where $p \in \Omega_{i,j}$ denotes pixel p in $\Omega_{i,j}$, and $\hat{d}_p$ denotes the direction vector at pixel p, which has been calculated in Step 1. $\text{mean}_{p \in \Omega_{i,j}}(\hat{d}_p)$ is the mean of the direction vectors for all pixels in $\Omega_{i,j}$, which can be represented by the means (denoted as $\bar{d}_x$ and $\bar{d}_y$) of the two orthogonal components (horizontal and vertical in the compass circle) of the direction vectors in $\Omega_{i,j}$. Then, $f(\Omega_{i,j}) = \bar{d}_x^2 + \bar{d}_y^2$.

Step 4: Find the candidate area with the minimum of the square of MMDV and set it to be the search area at the upper level of the pyramid (Ω_{i+1}). This operation can be written as follows:

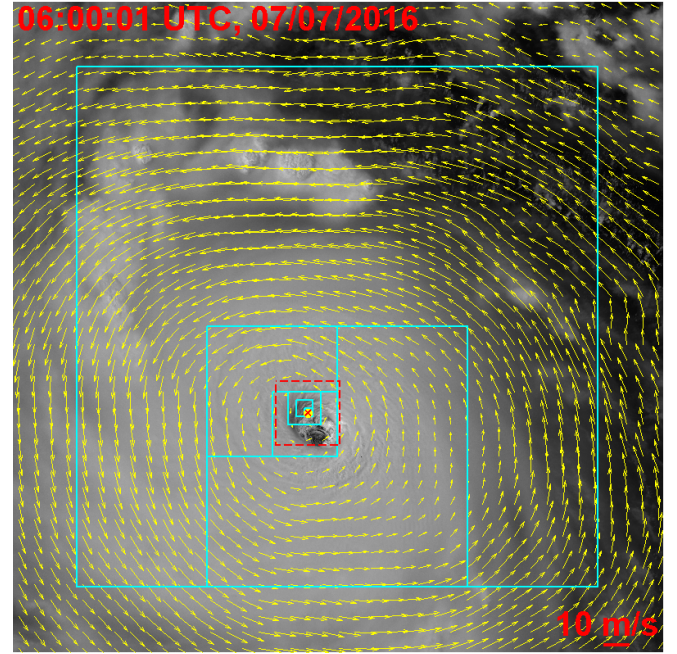$$j' = \underset{j}{\text{argmin}}\, f(\Omega_{i,j}) \tag{12}$$

Fig. 8.   Boxes (in cyan) of the search areas at each level illustrate the searching path from the bottom of the pyramid to the top until the TC center is located. The red box denotes the neighborhood of the MMDV-derived TC center for searching for the speed-adjusted TC center. The MMDV-derived TC center and the speed-adjusted TC center are denoted by yellow dot and red "×," respectively. Search of the MMDV-derived TC center in 10 240 × 10 240 AMVs takes 9 s in a desktop computer with CPU of E5-2630 v3 at 2.40 GHz and MATLAB R2015b.

$$\Omega_{i+1} = \Omega_{i,j'}. \tag{13}$$

Step 5: Repeat Steps 2 to 4. After each recursion, the search area Ω_i is reduced to a smaller area Ω_{i+1} that is 1/4 size of Ω_i. With the power of 2 reduction after each recursion, Ω_i will finally converge to an area with only 2×2 pixels. The center of this small area is determined as the MMDV-derived TC center.

Step 6 (Optional): Smooth the motion magnitude image in the neighborhood of the MMDV-derived TC center, and
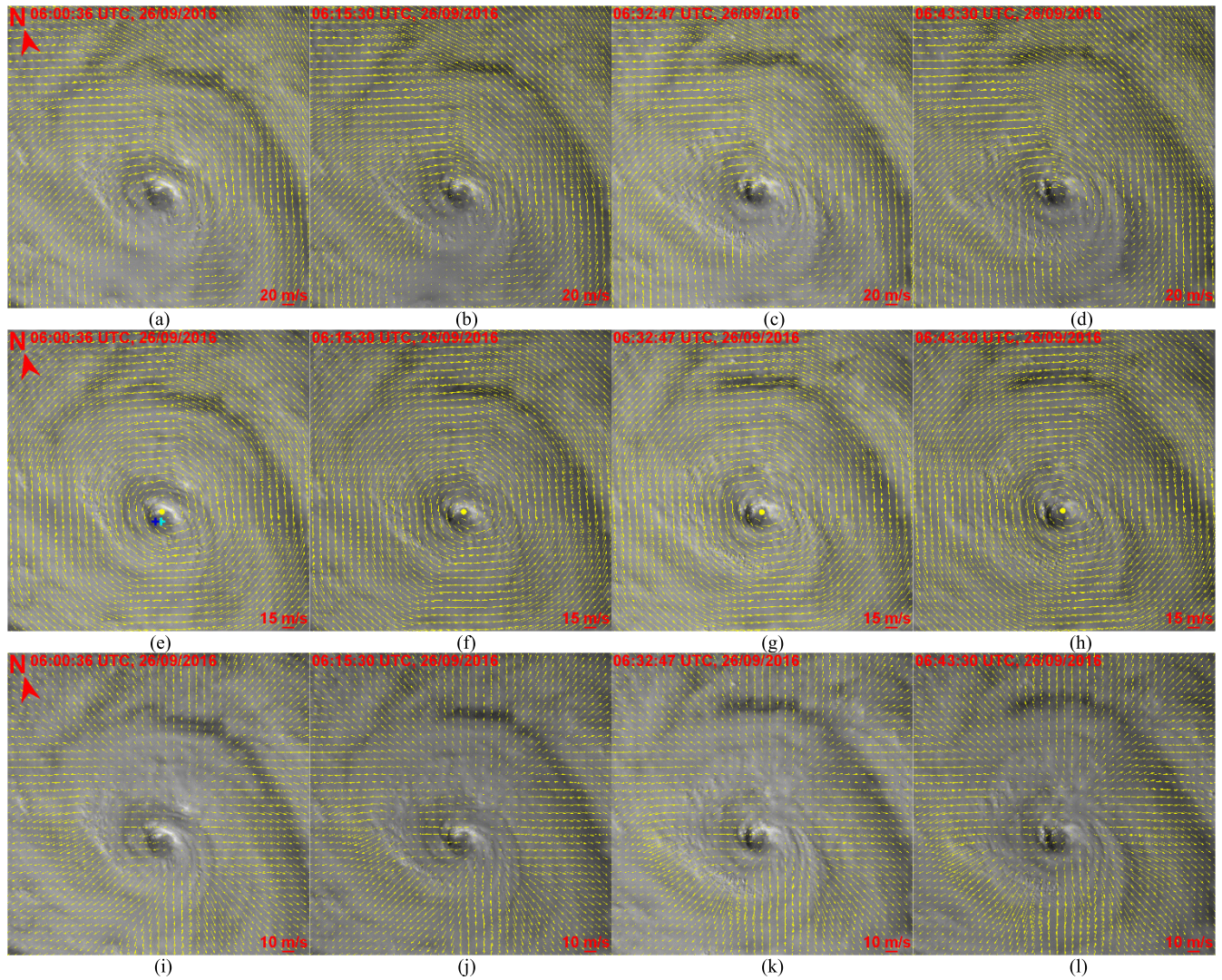
Fig. 9. Overview of the GF-4 image pairs of Typhoon Megi-2016 taken during 06:00:36 to 06:47:05 UTC on September 26, 2016, and the results of motion field decomposition and typhoon center determination. The background images are the master (first) images in the pairs. (a)–(d) Top cloud motion fields, (e)–(h) rotation components of top cloud motion fields, and (i)–(l) divergence components of top cloud motion fields. The MMDV-derived typhoon centers determined from the rotation components are denoted by yellow dots. The typhoon centers reported in the CMA, HKO, RSMC, and JTWC BT data sets are denoted by red, cyan, magenta, and blue "+" in (e), respectively. The typhoon centers reported in the CMA, RSMC, and JTWC BT data sets overlap at 06:00:00 UTC.

TABLE I
BT RECORDS OF THE MAXIMUM WIND SPEED AND CENTER PRESSURE OF MEGI-2016

UTC Time		Maximum Wind Speed (m/s)				Center Pressure (hPa)			
dd/mm	hh:mm	CMA	HKO	RSMC	JTWC	CMA	HKO	RSMC	JTWC
	06:00	45	46	36	51	950	945	960	948
26/09	12:00	45	46	36	54	950	945	960	944
	18:00	48	49	41	57	945	940	950	941
	00:00	52	49	44	59	940	940	945	937
27/09	06:00	45	46	41	51	950	945	950	948
	12:00	40	39	33	41	960	960	965	963
	18:00	35	36	28	31	970	965	975	978
28/09	00:00	28	28	23	28	985	980	985	981
	06:00	20	23	18	23	990	988	990	989

search for the location with minimum motion speed as the speed-adjusted TC center.

For clarity, the flowchart of the algorithm is summarized in Fig. 7.

Fig. 8 presents an example of locating the center of a TC in the rotation component of its cloud motion field using the algorithm described above. The cyan boxes define the search area at each level, and they illustrate the searching
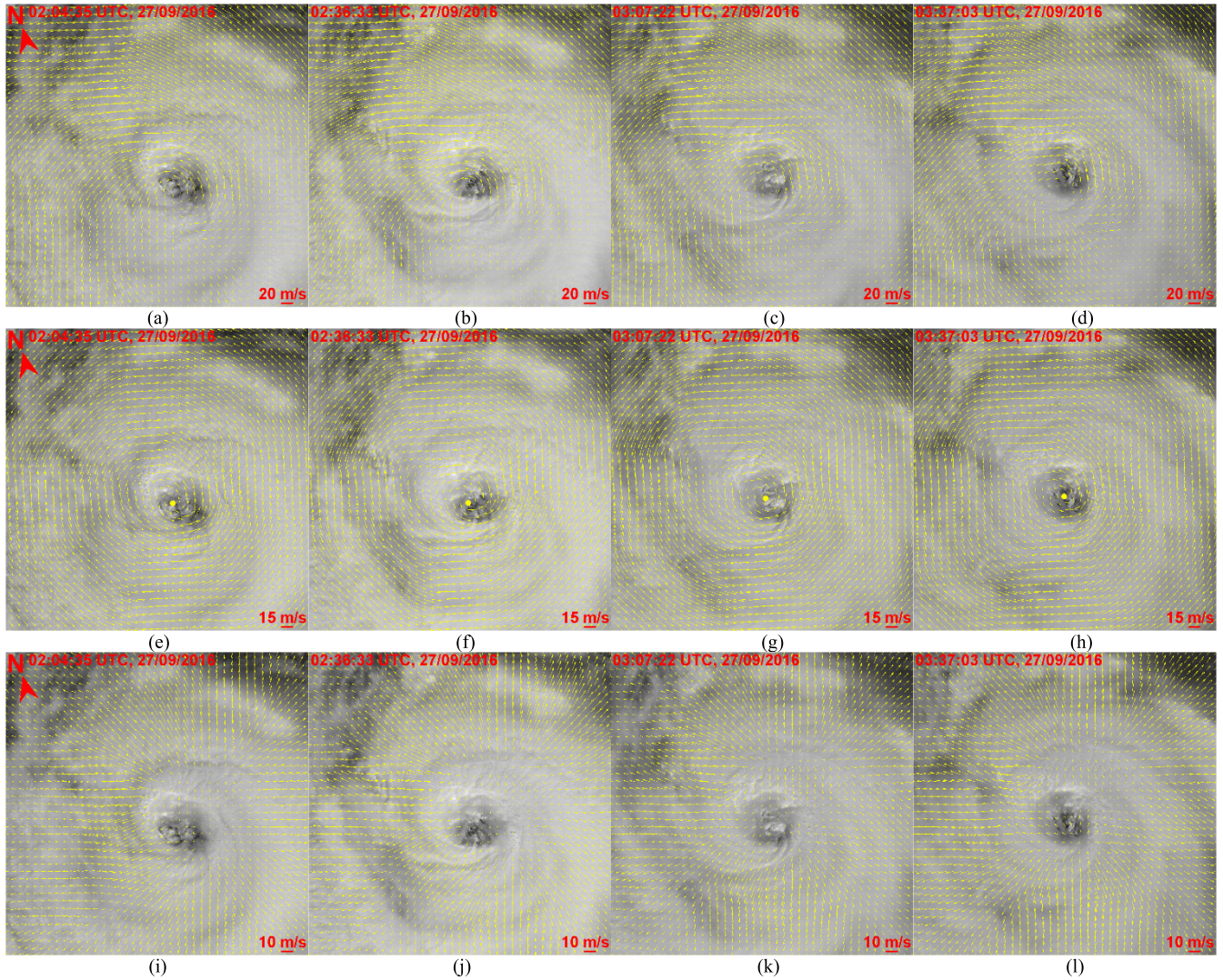
Fig. 10. Overview of the GF-4 image pairs of Typhoon Megi-2016 taken during 02:00:01 to 03:53:02 UTC on September 27, 2016, and the results of motion field decomposition and typhoon center determination. The background images are the master (first) images in the pairs. (a)–(d) Top cloud motion fields, (e)–(h) rotation components of top cloud motion fields, and (i)–(l) divergence components of top cloud motion fields. The MMDV-derived typhoon centers determined from the rotation components are denoted by yellow dots.

path from the bottom of the pyramid to the top until the TC center is located. The red box denotes the neighborhood of the MMDV-derived TC center for searching for the speed-adjusted TC center. The MMDV-derived TC center and the speed-adjusted TC center are denoted by a yellow dot and red × mark, respectively; they are usually close to each other.

IV. TEST AND ASSESSMENT

The automatic TC center determination algorithm based on the motion field decomposition has been tested using GF-4 images of several typhoons. The top cloud motion fields were generated by the PCIAS from consecutive image pairs and then decomposed by the proposed motion field decomposition in Section II-B. Considering that rotation is the main feature of a typhoon during most of its life cycle, the MMDV-derived typhoon centers were determined in the rotation components of the motion fields without applying the lowest speed-based adjustment.

For reference, the International Best Track Archive for Climate Stewardship (IBTrACS) version 3 was acquired. The data are provided by the National Centers for Environmental Information (NCEI), National Ocean and Atmospheric Administration (NOAA), College Park, MD, USA, including the best track (BT) data set of China Meteorological Administration (CMA)—Shanghai Typhoon Institute, the BT data set of Hong Kong Observatory (HKO), the BT data set of Regional Specialized Meteorological Center (RSMC) of Japan, and the BT data set of Joint Typhoon Warning Center (JTWC). The typhoon center location, maximum wind speed, and center pressure were normally reported every 6 h in these BT data sets.

A. Typhoon Megi-2016

Typhoon Megi (2016) was imaged by the GF-4 satellite in four periods: 06:00:36–06:47:05 UTC, September 26; 02:00:01–03:53:02 UTC, September 27; 05:00:01–06:53:02 UTC, September 27; and 03:12:34–04:41:37 UTC, September 28.
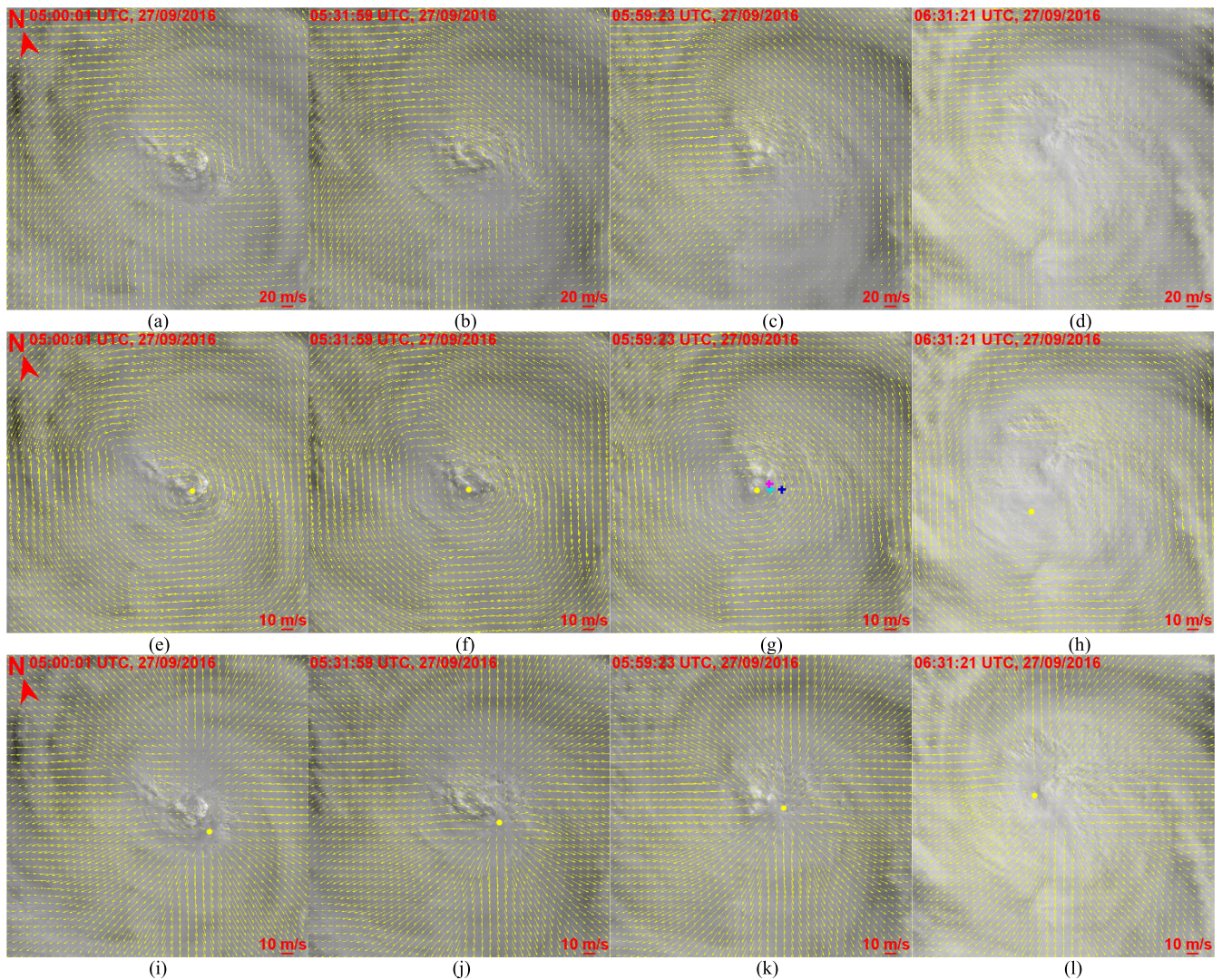
Fig. 11. Overview of the GF-4 image pairs of Typhoon Megi-2016 taken during 05:00:01 to 06:53:02 UTC on September 27, 2016, and the results of motion field decomposition and typhoon center determination. The background images are the master (first) images in the pairs. (a)–(d) Top cloud motion fields, (e)–(h) rotation components of top cloud motion fields, and (i)–(l) divergence components of top cloud motion fields. The MMDV-derived typhoon centers determined from the rotation and divergence components are denoted by yellow dots. The typhoon centers reported in the CMA, HKO, RSMC, and JTWC BT data sets are denoted by red, cyan, magenta, and blue "+" in (g), respectively. The typhoon centers reported in the CMA and HKO BT data sets overlap at 06:00:00 UTC.

During the first imaging period (06:00:36–06:47:05 UTC, September 26, 2016), 17 consecutive image pairs with a 179 or 180 s (six frames) interval from 76 images were processed. Fig. 9 presents part of them to illustrate the results of motion field decomposition and typhoon center determination. The yellow arrows denote the motion vectors. The background images are the master (first) GF-4 images of the pairs. The MMDV-derived typhoon centers determined from the rotation components are denoted by yellow dots in Fig. 9(e)–(h). For reference, the typhoon centers reported in the four BT datasets at 06:00 UTC are also shown in Fig. 9(e), and denoted by red, cyan, magenta, and blue "+" for CMA, HKO, RSMC, and JTWC data, respectively.

The GF-4 images show that during the first imaging period, Megi-2016 had already become a typhoon having a typical structure with a typhoon eye in the center, as a hole, and fast swirling clouds rotating anticlockwise around the eye forming a dish. The maximum wind speeds and center pressures at

06:00 and 12:00 UTC, September 26, 2016 (Table I) indicate that Megi-2016 was in steady status during the period. The motion fields overall present deformed concentric patterns with a low-speed area and a high-speed area appearing in the bottom and top-right parts of the scene. After the motion field decomposition, the concentric rotation is clearly shown in the rotation components. The rotation components are consistent with the spiral cloud structure in the corresponding GF-4 images, indicating an obvious rotation center with low motion speed surrounding the eye. The divergence components also indicate a radiation center slightly deviates from the eye. The MMDV-derived typhoon centers determined from the rotation components are in a good agreement with the visual observation of the typhoon eye and the BT records.

During the second imaging period (02:00:01–03:53:02 UTC, September 27, 2016), 27 consecutive image pairs with a 206 or 207 s (four frames) interval from 97 images were processed. Fig. 10 presents an overview of the results
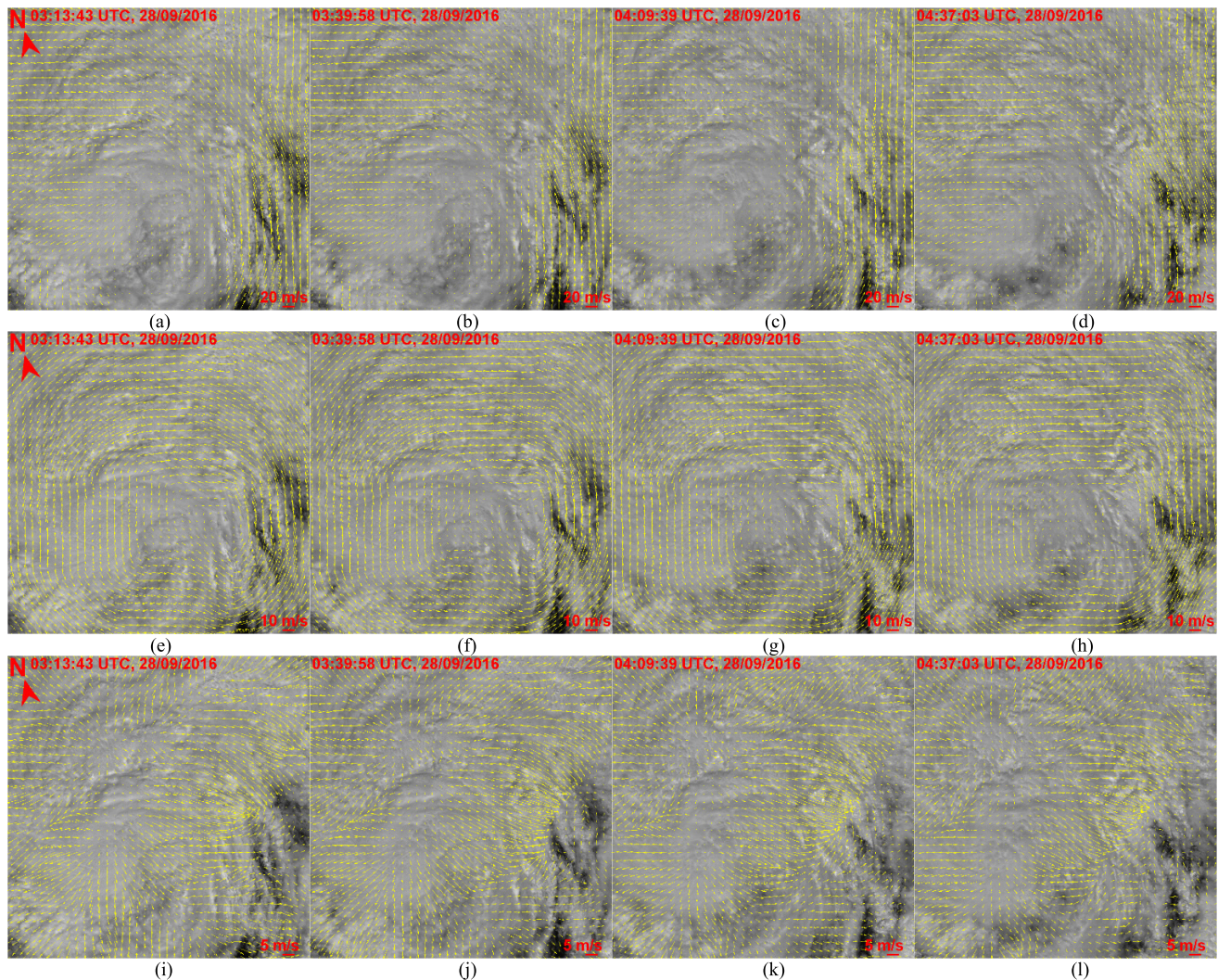
Fig. 12. Overview of the GF-4 image pairs of Typhoon Megi-2016 taken during 03:12:34 to 04:41:37 UTC on September 28, 2016, and the results of motion field decomposition. The background images are the master (first) images in the pair. (a)–(d) Top cloud motion fields, (e)–(h) rotation components of top cloud motion fields, and (i)–(l) divergence components of top cloud motion fields.

illustrated by part of the data. The GF-4 images show that during the second imaging period, Megi-2016 was still a cyclone dish with an eye. The maximum wind speeds and center pressures at 00:00 and 06:00 UTC, September 27, 2016 (Table I) indicate that the intensity of Megi-2016 was decreasing during the period. The motion fields present deformed concentric patterns with a low-speed area and a high-speed area appearing in the bottom-right and top-left parts of the scene. The rotation components of the motion fields, after decomposition, reveal more typical concentric rotation patterns with a well-defined rotation center of low motion speed. The divergence components show two radiation centers: one slightly deviates from the eye while the other is much farther away from the eye. The MMDV-derived typhoon centers determined from the rotation components are in a good agreement with the visually recognized eye positions in the GF-4 images.

During the third imaging period (05:00:01–06:53:02 UTC, September 27, 2016), Megi-2016 made landfall over the city of Hualien on Taiwan Island around 06:00 UTC. Twenty-six consecutive image pairs with a 206 or 207 s (four frames)

interval from 93 images were processed, and Fig. 11 presents an overview of the results illustrated by part of the data. The GF-4 images show that during the third period, Megi-2016 still has a spiral cloud structure but no eye anymore. The maximum wind speeds and center pressures at 00:00, 06:00, and 12:00 UTC, September 27, 2016 (Table I) indicate that the intensity of Megi-2016 decreased further during the period. Similar to the first and second periods, the motion fields also present deformed concentric patterns. The position of the center of the rotation component became unstable soon after the landfall (around 06:00 UTC) of Megi-2016. Complicated interaction between the typhoon and the high terrain relief (e.g., the Central Mountains) of Taiwan Island weakened the typhoon considerably. The MMDV-derived typhoon centers determined from the rotation components are shown in Fig. 11(e)–(h). The typhoon centers at 06:00 UTC, September 27, 2016, in the BT data sets are shown in Fig. 11(g) for reference, where we can see that the MMDV-derived typhoon center and the reported typhoon centers in the BT data sets are in a good agreement at the BT data point. The MMDV-derived centers from the divergence component are denoted in Fig. 11(i)–(l).
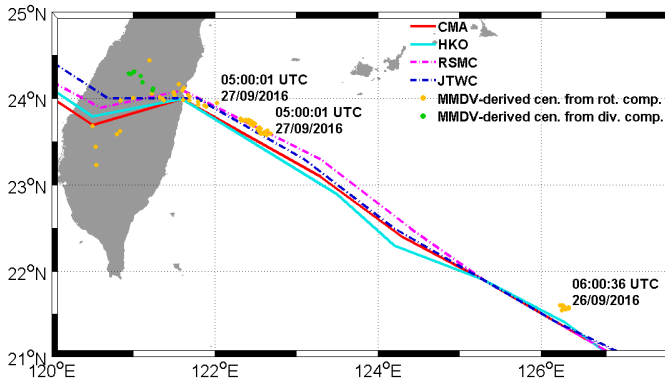
Fig. 13. MMDV-derived centers of Typhoon Megi-2016 from GF-4 images and the typhoon migration tracks in the BT data sets. The MMDV-derived centers are denoted by dots. The typhoon migration tracks in the CMA, HKO, RSMC, and JTWC BT data sets are denoted by red, cyan, magenta, and blue lines. The labeled times in the figure are the times of the first TC center locations at the beginning of the three imaging periods.

Comparison between Fig. 11(e)–(h) and (i)–(l) indicates that before the landfall the MMDV-derived center determined from the rotation component is visually more consistent with the center of the cloud pattern than that determined from the divergence component, but soon after the landfall the motion of the typhoon eye was dominated by radiation rather than rotation probably as the result of the interaction between the typhoon and the high relief terrain of the Central Mountains in Taiwan. In this case, the MMDV-derived TC centers from the divergence components are more consistent with the cloud patterns and the BT tracks than those from the rotation components.

Megi-2016 migrated across Taiwan Strait northwestward and made its second landfall over Hui'an County of Quanzhou City around 20:40 UTC, September 27, 2016. The fourth imaging period (03:12:34–04:41:37 UTC, September 28, 2016) was after the second landfall. Twenty-four consecutive image pairs with a 206 or 207 s (four frames) interval from 78 images were processed, and Fig. 12 presents part of them to illustrate an overview of the motion fields and their rotation and divergence components. From the background images in Fig. 12, we can see the cloud structures did not have an eye and nor any obvious concentric feature during the period. The maximum wind speeds and center pressures at 00:00 and 06:00 UTC, September 28, 2016 (Table I) indicate that Megi-2016 had degraded to a tropical storm during the period. The cloud structures and motion fields show no obvious rotation centers, and Megi-2016 was approaching its end. We did not locate the center of Megi-2016 system during this period.

The MMDV-derived centers of Typhoon Megi-2016 determined from consecutive GF-4 image pairs of the first three imaging periods and the typhoon migration tracks reported in the four BT data sets are shown in Fig. 13. The MMDV-derived typhoon centers are denoted by yellow dots, and the typhoon migration tracks in the CMA, HKO, RSMC, and JTWC BT data sets are denoted by red, cyan, magenta, and blue lines. Because the first imaging period was short, and the migration speed of Megi-2016 was low during the period

(about 5 m/s estimated from the BT data sets), the centers cluster at the bottom-right corner of Fig. 13 around 21.58°N, 126.29°E. The centers determined from the rotation components show a marginal linear migration track of Megi-2016 before the landfall over Hualien City, and this track is in a good agreement with those in the BT data sets. After the landfall, the detailed center positions determined from the rotation components of typhoon top cloud motion fields using the MMDV method become scattered though they overall match the migration tracks of the BT records. As shown in Fig. 13, the scattered rotation centers imply a drastic jump in the position of the typhoon center. This revealing phenomenon is interesting and needs further investigation and verification. We reckon that the drastic jumping of the center after the landfall was an internal structural variation inside the typhoon system possibly in response to the topography of the Central Mountains, while the typhoon system as a whole did not jump and remain its steady trajectory toward the west. As indicated before, the divergence component still kept its strength while the rotation component weakened. Thus, for this imaging period, the MMDV-derived centers were also determined from the radiation components and are denoted by green dots in Fig. 13, which are less scattered.

B. Other Typhoons

For further verification, the proposed MMDV-pyramid searching method for TC center determination has also been tested with the GF-4 cloud images of other five typhoons (Nepartak-2016, Sarika-2016, Haima-2016, Nesat-2017, and Talim-2017). Fig. 14 shows the diverse cloud patterns of these typhoons with or without eyes. The optical flow of the rotation components of the cloud motion fields derived from GF-4 image pairs is presented by yellow arrows with the MMDV-derived rotation centers denoted as yellow dots. The typhoon centers reported in the CMA, HKO, RSMC, and JTWC BT data sets are also shown in Fig. 14(b) and (c) for reference, which are denoted by red, cyan, magenta, and blue "+," respectively. We can see that the MMDV-derived centers are in accordance with the cloud pattern centers in a visual sense and also with the reported TC centers in the BT datasets. The results demonstrate the effectiveness and robustness of the method that works well for typhoon systems with a great diversity of spatial patterns, even for the very complicated case, as shown in Fig. 14(k). According to our experiments, we are confident that the proposed method can reliably locate the TC rotation center as long as the rotation motion is dominant in a cloud feature system. This is fundamentally different from the static image feature-based methods that rely on recognizing spiral structures based on cloud feature patterns.

C. Speed-Adjusted Centers

Fig. 15 presents two examples of speed-adjusted centers determined from rotation components of motion fields, as marked by green "×," in comparison with the MMDV-derived centers marked by yellow dots. In almost all the image pairs that we tested, speed-adjusted centers and
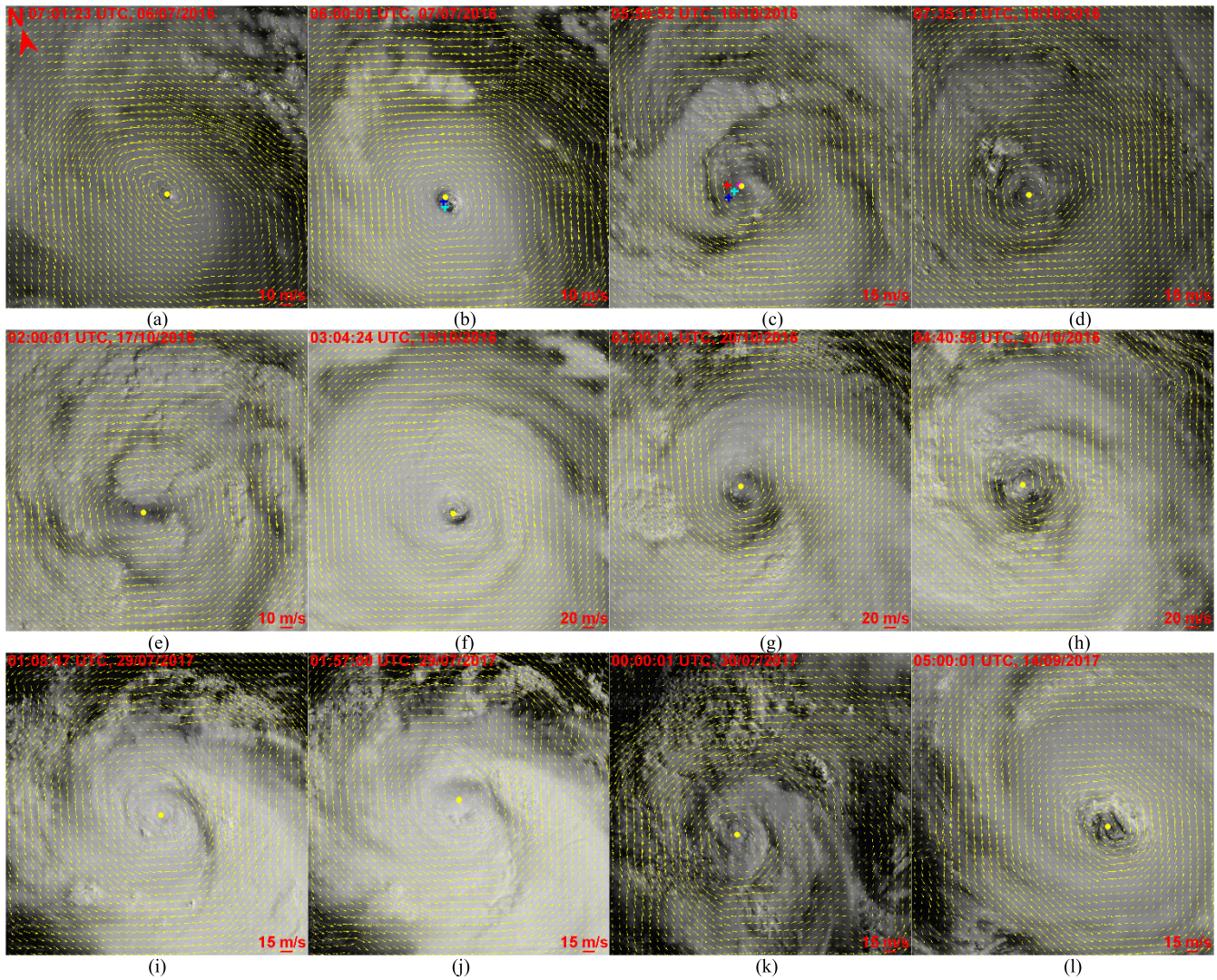
Fig. 14. Rotation components of top cloud motion fields of five typhoons and the MMDV-derived typhoon centers determined from the rotation components are denoted by yellow arrows and dots. The typhoon centers reported in the CMA, HKO, RSMC, and JTWC BT data sets are also shown in (b) and (c) for reference, which are denoted with red, cyan, magenta, and blue "+," respectively. The typhoon centers of Nepartak reported in the CMA, RSMC, and JTWC BT data sets overlap at 06:00:00 UTC, July 7, 2016. (a) and (b) Nepartak-2016, (c)–(e) Sarika-2016, (f)–(h) Haima-2016, (i)–(k) Nesat-2017, and (l) Talim-2017.
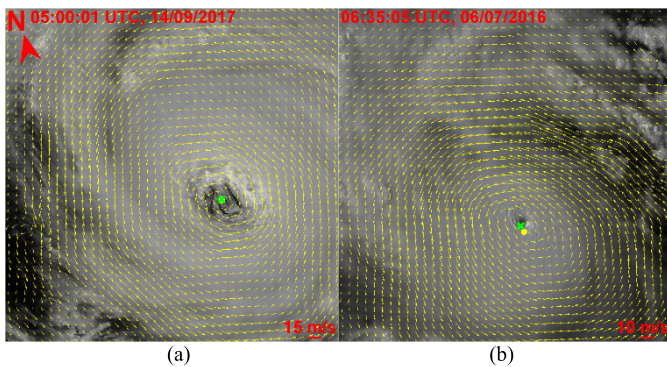

Fig. 15. In almost all the cases that we tested, (a) MMDV-derived centers (yellow dots) and speed-adjusted centers (green "×") nearly overlap, and (b) in a few cases, they are apart in very small differences.

MMDV-derived centers nearly overlap like in Fig. 15(a), and only in a few cases speed-adjusted centers deviate slightly from MMDV-derived centers like in Fig. 15(b). This is in accordance with the fact that at the rotation center of a typhoon, the speed in the rotation plane is minimum.

V. CONCLUSION

The Chinese GF-4 geostationary satellite is capable of capturing top cloud motions of TCs in the panchromatic band with high resolution of 50 m, wide coverage of 512 km × 512 km, and high imaging rate as frequent as 20 s. Such powerful imaging capability enables derivation of TC top-cloud motion AMV data at unprecedented high tempo-spatial resolution. The new data triggered our development of a new method to automatically and accurately determine TC centers based on cloud concentric motion, as presented in this article. The processing procedure of the method comprises three parts.

1) Generating the pixel-wise motion fields of TCs from pairs of consecutive GF-4 image using our advanced PC image matching software with subpixel accuracy.

2) A refined motion field decomposition with a physics-based meaningful constraint is designed to decompose a motion field to rotation and divergence components and meanwhile remove all possible translational components, including both TC migration and scene shift, without introducing artifacts as did by the previously published decomposition algorithm.

3) Considering that rotation is the diagnostic feature of a TC during most of its life cycle, its center can be determined based on the rotation component of its motion field. Thus, a rotation center locating method based on a simple indicator (MMDV) executed with a pyramid search scheme is developed to effectively locate rotation center by using motion direction information in the rotation component extracted via the decomposition of cloud motion field data. For further refinement, the location with the minimum motion speed in the neighborhood of the MMDV-derived center can be searched to adjust the position and called speed-adjusted center.

The above TC center determination method has been tested using the GF-4 images of six typhoons. TC centers are accurately tracked in all cases. For almost all cases, the MMDV-derived and speed-adjusted typhoon centers entirely or nearly overlap; this is in accordance with our intuition that the rotation center of a typhoon is also the location with minimum motion speed in the rotation plane. The located typhoon centers are in good agreement with cloud pattern centers in a visual sense and also with those reported in the four BT datasets of CMA, HKO, RSMC, and JTWC. However, the dense TC center data that we derived reveal that after landfall of a typhoon, the position of the typhoon rotation center can become scattered as the case of the Megi-2016 landfall over the city of Hualien on Taiwan Island. The phenomenon may have resulted from the interaction between the typhoon and the high terrain relief of the Taiwan Central Mountains. Further investigation is pending.

In fact, conventional methods such as manual recognition via visual interpretation could achieve higher accuracy in some cases but often subject to human errors. Our technique can fully automatically and accurately locate the TC centers, and the results are consistent with visual assessment in most cases. The process is efficient, objective, and repeatable.

For the purpose of automatic tracking a TC, many short imaging periods with high imaging rates are preferable than a few long periods. Decreasing the length of the imaging period but increasing the number of periods could be a more effective and economic imaging process for typhoon monitoring.

APPENDIX

Using the Green function (denoted as g) of Poisson equation in free space, Ψ and χ in Ω can be written as follows:

$$\psi = \text{P.V.} \iint_\Omega g \hat{z} \cdot \nabla \times \vec{V} d\Omega' \quad (A1)$$

$$\chi = \text{P.V.} \iint_\Omega g \nabla \cdot \vec{V} d\Omega' \quad (A2)$$

where P.V. denotes Cauchy principal value, and g is

$$g(\vec{r}, \vec{r}') = \ln |\vec{r} - \vec{r}'|/2\pi + c \quad (A3)$$

where $|\cdot|$ denotes vector magnitude. $\vec{r}$ denotes position vectors, and c is a constant.

Applying (A1)–(A3) to (2)–(3) gives

$$\vec{V}_\psi = \frac{1}{2\pi} \text{P.V.} \iint_\Omega \hat{z} \times \frac{\vec{r} - \vec{r}'}{|\vec{r} - \vec{r}'|^2} \hat{z} \cdot \nabla \times \vec{V} d\Omega' \quad (A4)$$

$$\vec{V}_\chi = \frac{1}{2\pi} \text{P.V.} \iint_\Omega \frac{\vec{r} - \vec{r}'}{|\vec{r} - \vec{r}'|^2} \nabla \cdot \vec{V} d\Omega'. \quad (A5)$$

Equations (A4) and (A5) are physical constrain. $(1)/(2\pi)\hat{z} \times (\vec{r} - \vec{r}')/(|\vec{r} - \vec{r}'|^2)$ and $(1)/(2\pi)(\vec{r} - \vec{r}')/(|\vec{r} - \vec{r}'|^2)$ are the rotation and radiation fields in free space derived from rotation and divergence point sources at position $\vec{r}'$. $\vec{V}_\psi$ and $\vec{V}_\chi$ are the rotation and divergence components of $\vec{V}$ derived from the distributed rotation and divergence sources (i.e., $\hat{z} \times \nabla \times \vec{V} d\Omega'$ and $\nabla \cdot \vec{V} d\Omega'$) inside Ω. Thus, the motions of rotation and divergence inside Ω are extracted. The residual $\vec{V}_0$ of Ω after the extraction of $\vec{V}_\psi$ and $\vec{V}_\chi$ is curl- and divergence-free, which includes both TC migration and scene shift without any contribution to $\vec{V}_\psi$ and $\vec{V}_\chi$ according to (A4) and (A5).

Equations (A4) and (A5) can be simplified to (6) and (7) for calculating $\vec{V}_\psi$ and $\vec{V}_\chi$ at the center of the pixel (m, n).

REFERENCES

[1] J. Chan and J. Kepert, Eds., "Tropical cyclone structure and dynamics," in *Global Perspectives of Tropical Cyclones*, 3rd ed. Singapore: World Scientific, 2010, pp. 201–226.

[2] K. Emanuel, "Increasing destructiveness of tropical cyclones over the past 30 years," *Nature*, vol. 436, pp. 686–688, Aug. 2005.

[3] P. J. Webster, G. J. Holland, J. A. Curry, and H.-R. Chang, "Changes in tropical cyclone number, duration, and intensity in a warming environment," *Science*, vol. 309, no. 5742, pp. 1844–1846, 2005.

[4] J. B. Elsner, J. P. Kossin, and T. H. Jagger, "The increasing intensity of the strongest tropical cyclones," *Nature*, vol. 455, no. 4, pp. 92–95, Sep. 2008.

[5] M. A. Bender *et al.*, "Modeled impact of anthropogenic warming on the frequency of intense Atlantic hurricanes," *Science*, vol. 327, no. 5964, pp. 454–458, Jan. 2010.

[6] T. R. Knutson *et al.*, "Tropical cyclones and climate change," *Nature Geosci.*, vol. 3, pp. 157–163, Mar. 2010.

[7] M. Sugi and J. Yoshimura, "Decreasing trend of tropical cyclone frequency in 228-year high-resolution AGCM simulations," *Geophys. Res. Lett.*, vol. 39, no. 19, Oct. 2012. doi: 10.1029/2012GL053360.

[8] R. Bell, J. Strachan, P. L. Vidale, K. Hodges, and M. Roberts, "Response of tropical cyclones to idealized climate change experiments in a global high-resolution coupled general circulation model," *J. Climate*, vol. 26, no. 20, pp. 7980–7996, Oct. 2013.

[9] N. Jaiswal and C. M. Kishtawal, "Objective detection of center of tropical cyclone in remotely sensed infrared images," *IEEE J. Sel. Topics Appl. Earth Observ. Remote Sens.*, vol. 6, no. 2, pp. 1031–1035, Apr. 2013.

[10] A. J. Wimmers and C. S. Velden, "Advancements in objective multisatellite tropical cyclone center fixing," *J. Appl. Meteorol. Climatol.*, vol. 55, no. 1, pp. 197–212, Jan. 2016.

[11] Q. Xu, G. Zhang, X. Li, and Y. Cheng, "An automatic method for tropical cyclone center determination from SAR," in *Proc. IEEE Int. Geosci. Remote Sens. Symp.*, Beijing, China, Jul. 2016, pp. 2250–2252. doi: 10.1109/IGARSS.2016.7729581.

[12] T. Hu *et al.*, "Study on typhoon center monitoring based on HY-2 and FY-2 data," *IEEE Geosci. Remote Sens. Lett.*, vol. 14, no. 12, pp. 2350–2354, Dec. 2017.

[13] S. Jin, S. Wang, X. Li, L. Jiao, J. A. Zhang, and D. Shen, "A salient region detection and pattern matching-based algorithm for center detection of a partially covered tropical cyclone in a SAR image," *IEEE Trans. Geosci. Remote Sens.*, vol. 55, no. 1, pp. 280–291, Jan. 2017.

[14] X. Lu, H. Yu, X. Yang, and X. Li, "Estimating tropical cyclone size in the Northwestern Pacific from Geostationary satellite infrared images," *Remote Sens.*, vol. 9, no. 7, p. 728, 2017. doi: 10.3390/rs9070728.

[15] W. Yanyan, W. Han, C. Hong, and S. Wei-Chi, "Tropical cyclone center location with digital image process," in *Proc. Int. Conf. Info-Tech Info-Net*, Beijing, China, Oct./Nov. 2001, pp. 563–567. doi: 10.1109/ICII.2001.983116.

[16] W. K. Yan, Y. C. Lap, and L. P. Wah, "Automatic tropical cyclone eye fix using genetic algorithm," *Expert Syst. Appl.*, vol. 34, no. 1, pp. 643–656, Jan. 2008.

[17] N. Jaiswal and C. M. Kishtawal, "Automatic determination of center of tropical cyclone in satellite-generated IR images," *IEEE Geosci. Remote Sens. Lett.*, vol. 8, no. 3, pp. 460–463, May 2011.

[18] K. Wei and Z.-L. Jing, "Spiral band model optimization by chaos immune evolutionary algorithm for locating tropical cyclones," *Atmos. Res.*, vol. 97, nos. 1–2, pp. 266–277, Jul. 2010.

[19] S. Chaurasia, C. M. Kishtawal, and P. K. Pal, "An objective method of cyclone centre determination from geostationary satellite observations," *Int. J. Remote Sens.*, vol. 31, no. 9, pp. 2429–2440, 2010.

[20] M. F. Pineros, E. A. Ritchie, and J. S. Tyo, "Objective measures of tropical cyclone structure and intensity change from remotely sensed infrared image data," *IEEE Trans. Geosci. Remote Sens.*, vol. 46, no. 11, pp. 3574–3580, Nov. 2008.

[21] T.-L. Pao and J.-H. Yeh, "Typhoon locating and reconstruction from the infrared satellite cloud image," *J. Multimedia*, vol. 3, no. 2, pp. 45–51, Jun. 2008.

[22] K. S. Friedman and X. Li, "Monitoring hurricanes over the ocean with wide swath SAR," in *Johns Hopkins APL Tech. Dig.*, 2000, vol. 21, no. 1, pp. 80–85.

[23] Y.-H. Cheng, S.-J. Huang, A. K. Liu, C.-R. Ho, and N.-J. Kuo, "Observation of typhoon eyes on the sea surface using multi-sensors," *Remote Sens. Environ.*, vol. 123, pp. 434–442, Aug. 2012.

[24] B. Zhang *et al.*, "Ocean vector winds retrieval from C-band fully polarimetric SAR measurements," *IEEE Trans. Geosci. Remote Sens.*, vol. 50, no. 11, pp. 4252–4261, Nov. 2012.

[25] X. Li *et al.*, "Tropical cyclone morphology from spaceborne synthetic aperture radar," *Bull. Amer. Meteorol. Soc.*, vol. 94, no. 2, pp. 215–230, Feb. 2013.

[26] X. Zhou *et al.*, "Estimation of tropical cyclone parameters and wind fields from SAR images," *Sci. China, Earth Sci.*, vol. 56, no. 11, pp. 1977–1987, Jun. 2013.

[27] P. A. Hwang, W. Perrie, and B. Zhang, "Cross-polarization radar backscattering from the ocean surface and its dependence on wind velocity," *IEEE Geosci. Remote Sens. Lett.*, vol. 11, no. 12, pp. 2188–2192, Dec. 2014.

[28] S. Jin, S. Wang, and X. Li, "Typhoon eye extraction with an automatic SAR image segmentation method," *Int. J. Remote Sens.*, vol. 35, nos. 11–12, pp. 3978–3993, 2014.

[29] I. K. Lee, A. Shamsoddini, X. Li, J. C. Trinder, and Z. Li, "Extracting hurricane eye morphology from spaceborne SAR images using morphological analysis," *ISPRS J. Photogramm. Remote Sens.*, vol. 117, pp. 115–125, Jul. 2016.

[30] G. Zheng, J. Yang, A. K. Liu, X. Li, W. G. Pichel, and S. He, "Comparison of typhoon centers from SAR and IR images and those from best track data sets," *IEEE Trans. Geosci. Remote Sens.*, vol. 54, no. 2, pp. 1000–1012, Feb. 2016.

[31] P. Hwang, X. Li, and B. Zhang, "Retrieving hurricane wind speed from dominant wave parameters," *IEEE J. Sel. Topics Appl. Earth Observ. Remote Sens.*, vol. 10, no. 6, pp. 2589–2598, Jun. 2017.

[32] W. Shao, X. Li, P. Hwang, B. Zhang, and X. Yang, "Bridging the gap between cyclone wind and wave by C-band SAR measurements," *J. Geophys. Res., Ocean*, vol. 122, pp. 6714–6724, Jul. 2017.

[33] G. Zhang, W. Perrie, X. Li, and J. A. Zhang, "A hurricane morphology and sea surface wind vector estimation model based on C-band cross-polarization SAR imagery," *IEEE Trans. Geosci. Remote Sens.*, vol. 55, no. 3, pp. 1743–1751, Mar. 2017.

[34] G. Zhang, X. Li, W. Perrie, P. A. Hwang, B. Zhang, and X. Yang, "A hurricane wind speed retrieval model for C-band RADARSAT-2 cross-polarization ScanSAR images," *IEEE Trans. Geosci. Remote Sens.*, vol. 55, no. 8, pp. 4766–4774, Aug. 2017.

[35] K. Y. Wong and C. L. Yip, "Identifying centers of circulating and spiraling vector field patterns and its applications," *Pattern Recognit.*, vol. 42, no. 7, pp. 1371–1387, 2009.

[36] J. A. Leese, C. S. Novak, and V. R. Taylor, "The determination of cloud pattern motions from geosynchronous satellite image data," *Pattern Recognit.*, vol. 2, no. 4, pp. 279–280, 1970.

[37] R. H. Langland, C. Velden, P. M. Pauley, and H. Berger, "Impact of satellite-derived rapid-scan wind observations on numerical model forecasts of Hurricane Katrina," *Monthly Weather Rev.*, vol. 137, no. 5, pp. 1615–1622, May 2009.

[38] M. Cordoba, S. L. Dance, G. A. Kelly, N. K. Nichols, and J. A. Waller, "Diagnosing atmospheric motion vector observation errors for an operational high-resolution data assimilation system," *Quart. J. Roy. Meteorol. Soc.*, vol. 143, no. 702, pp. 333–341, Jan. 2017.

[39] K. M. Bedka, C. S. Velden, R. A. Petersen, and W. F. Feltz, "Comparisons of satellite-derived atmospheric motion vectors, rawinsondes, and NOAA wind profiler observations," *J. Appl. Meteorol. Climate*, vol. 48, pp. 1542–1561, Aug. 2009.

[40] M. Otsuka, M. Kunii, H. Seko, K. Shimoji, M. Hayashi, and K. Yamashita, "Assimilation experiments of MTSAT rapid scan atmospheric motion vectors on a heavy rainfall event," *J. Meteorol. Soc. Jpn.*, vol. 93, no. 4, pp. 459–475, Sep. 2015.

[41] A. F. Hasler, K. Palaniappan, C. Kambhammetu, P. Black, E. Uhlhorn, and D. Chesters, "High-resolution wind fields within the inner core and eye of a mature tropical cyclone from GOES 1-min images," *Bull. Amer. Meteorol. Soc.*, vol. 79, no. 11, pp. 2483–2496, Nov. 1998.

[42] C. Velden *et al.*, "Recent innovations in deriving tropospheric winds from meteorological satellites," *Bull. Amer. Meteorol. Soc.*, vol. 86, no. 2, pp. 205–223, Feb. 2005.

[43] E. Rodgers, R. C. Gentry, and W. Shenk, "The benefits of using short-interval satellite images to derive winds for tropical cyclones," *Monthly Weather Rev.*, vol. 107, no. 5, pp. 575–584, May 1979.

[44] E. Rodgers and R. C. Gentry, "Monitoring tropical-cyclone intensity using environmental wind fields derived from short-interval satellite images," *Monthly Weather Rev.*, vol. 111, no. 5, pp. 979–996, May 1983.

[45] T. T. Fujita, K. Watanabe, and T. Izawa, "Formation and structure of equatorial anticyclones caused by large-scale cross-equatorial flows determined by ATS-I photographs," *J. Appl. Meteor.*, vol. 8, no. 4, pp. 649–667, Aug. 1969.

[46] J. A. Leese, C. S. Clark, and C. S. Novak, "An automated technique for obtaining cloud motion from Geosynchronous satellite data using cross correlation," *J. Appl. Meteorol.*, vol. 10, no. 1, pp. 118–132, Feb. 1971.

[47] C. M. Kishtawal, S. K. Deb, P. K. Pal, and P. C. Joshi, "Estimation of atmospheric motion vectors from Kalpana-1 imagers," *J. Appl. Meteor. Climate*, vol. 48, no. 11, pp. 2410–2421, Nov. 2009.

[48] W. D. Robinson, B. A. Franz, A. Mannino, and J.-H. Ahn, "Cloud motion in the GOCI/COMS ocean colour data," *Int. J. Remote Sens.*, vol. 37, no. 20, pp. 4948–4963, 2016.

[49] R. M. Endlich, D. E. Wolf, D. J. Hall, and A. E. Brain, "Use of a pattern recognition technique for determining cloud motions from sequences of satellite photographs," *J. Appl. Meteorol.*, vol. 10, pp. 105–117, Feb. 1971.

[50] D. E. Wolf, D. J. Hall, and R. M. Endlich, "Experiments in automatic cloud tracking using SMS-GOES data," *J. Appl. Meteorol.*, vol. 16, no. 11, pp. 1219–1230, Nov. 1977.

[51] R. M. Endlich and D. E. Wolf, "Automatic cloud tracking applied to GOES and METEOSAT observations," *J. Appl. Meteorol.*, vol. 20, no. 3, pp. 309–319, Mar. 1981.

[52] W. Bresky and J. Daniels, "The feasibility of an optical flow algorithm for estimating atmospheric motion," in *Proc. 8th Int. Winds Workshop*, Beijing, China, 2006, pp. 24–28. [Online]. Available: https://pdfs.semanticscholar.org/5aff/3ea2151b44e8f34a405fdccda13aff05c62c.pdf

[53] Z. Peng, D. Yu, D. Huang, J. Heiser, and P. Kalb, "A hybrid approach to estimate the complex motions of clouds in sky images," *Sol. Energy*, vol. 138, pp. 10–25, Nov. 2016.

[54] Q. Wu, H.-Q. Wang, Y.-J. Lin, Y.-Z. Zhuang, and Y. Zhang, "Deriving AMVs from geostationary satellite images using optical flow algorithm based on polynomial expansion," *J. Atmos. Oceanic. Technol.*, vol. 33, no. 8, pp. 1727–1747, Aug. 2016.

[55] J. G. Liu, P. J. Mason, and J. Ma, "Measurement of the left-lateral displacement of Ms 8.1 Kunlun earthquake on 14 November 2001 using Landsat-7 ETM+ imagery," *Int. J. Remote Sens.*, vol. 27, no. 10, pp. 1891–1975, 2006.

[56] J. G. Liu and H. Yan, "Phase correlation pixel-to-pixel image co-registration based on optical flow and median shift propagation," *Int. J. Remote Sens.*, vol. 29, no. 20, pp. 5943–5956, 2008.

[57] G. L. K. Morgan, J. G. Liu, and H. Yan, "Precise subpixel disparity measurement from very narrow baseline stereo," *IEEE Trans. Geosci. Remote Sens.*, vol. 48, no. 9, pp. 3424–3433, Sep. 2010.

[58] M. Wang, Y. Cheng, X. Chang, S. Jin, and Y. Zhu, "On-orbit geometric calibration and geometric quality assessment for the high-resolution geostationary optical satellite GaoFen4," *ISPRS J. Photogramm. Remote Sens.*, vol. 125, pp. 63–77, Mar. 2017.

[59] F. Sun, M. Min, D. Qin, F. Wang, and J. Hu, "Refined typhoon geometric center derived from a high spatiotemporal resolution geostationary satellite imaging system," *IEEE Geosci. Remote Sens. Lett.*, vol. 16, no. 4, pp. 499–503, Apr. 2019.

[60] J. Liu, G. Zheng, J. Yang, and J. Wang, "Top cloud motion field of typhoon megi-2016 revealed by GF-4 images," *IEEE Trans. Geosci. Remote Sens.*, vol. 57, no. 7, pp. 4427–4444, Jul. 2019.

[61] H. S. Stone, M. T. Orchard, E.-C. Chang, and S. A. Martucci, "A fast direct Fourier-based algorithm for subpixel registration of images," *IEEE Trans. Geosci. Remote Sens.*, vol. 39, no. 10, pp. 2235–2243, Oct. 2001.

[62] H. Foroosh, J. B. Zerubia, and M. Berthod, "Extension of phase correlation to subpixel registration," *IEEE Trans. Image Process.*, vol. 11, no. 3, pp. 188–200, Mar. 2002.

[63] W. S. Hoge, "A subspace identification extension to the phase correlation method [MRI application]," *IEEE Trans. Med. Imag.*, vol. 22, no. 2, pp. 277–280, Feb. 2003.

[64] J. G. Liu, H. Yan, and G. Morgan, "PCIAS subpixel technology," *Meas. Control*, vol. 45, no. 7, pp. 207–211, Sep. 2012.

[65] X. Wan, J. Liu, H. Yan, and G. L. Morgan, "Illumination-invariant image matching for autonomous UAV localisation based on optical sensing," *ISPRS J. Photogramm. Remote Sens.*, vol. 119, pp. 198–213, Sep. 2016.

[66] C. D. Kuglin and D. C. Hines, "The phase correlation image alignment method," in *Proc. Int. Conf. Soc.*, 1975, pp. 163–165.

[67] D. G. Lowe, "Object recognition from local scale-invariant features," in *Proc. 7th IEEE Int. Conf. Comp. Vis.*, Kerkyra, Greece, Sep. 1999, pp. 1150–1157. doi: 10.1109/ICCV.1999.790410.

[68] H. Bay, A. Ess, T. Tuytelaars, and L. Van Gool, "Speeded-up robust features (SURF)," *Comput. Vis. Image Understand.*, vol. 110, no. 3, pp. 346–359, 2008.

[69] P. Lynch, "Partitioning the wind in a limited domain," *Monthly Weather Rev.*, vol. 117, no. 7, pp. 1492–1500, Jul. 1989.

Jianguo Liu (M'10) received the M.Sc. degree in remote sensing and geology from the China University of Geosciences, Beijing, China, in 1982, and the Ph.D. degree in remote sensing and image processing from Imperial College London, London, U.K., in 1991.

He is currently a Reader of remote sensing with the Department of Earth Science and Engineering, Imperial College London, and a Distinguished Visiting Ocean Star Scholar with the State Key Laboratory of Satellite Ocean Environment Dynamics, Second Institute of Oceanography, Ministry of Natural Resources, Hangzhou, China. He has coauthored two books on remote sensing and authored over 130 research articles. His research interests include subpixel technology for image registration, 3-D and motion data generation, change detection, image processing techniques for data fusion, filtering and InSAR, and GIS multidata modeling for geohazard studies.

Jingsong Yang received the B.S. degree in physics and the M.S. degree in theoretical physics from Zhejiang University, Hangzhou, China, in 1990 and 1996, respectively, and the Ph.D. degree in physical oceanography from the Ocean University of China, Qingdao, China, in 2001.

Since 1996, he has been with the State Key Laboratory of Satellite Ocean Environment Dynamics, Second Institute of Oceanography (SIO), Ministry of Natural Resources, Hangzhou, where he is currently the Head of microwave marine remote sensing. Since 2002, he has been a Supervisor of graduate students with SIO and since 2011, he has been an Adjunct Professor and a Doctoral Supervisor with Zhejiang University. He has more than 20 years' experience in microwave marine remote sensing. He has been a Principal Investigator and a Participant of more than 20 research projects. He has authored more than 100 scientific papers in peer-reviewed journals and international conference proceedings. His research interests include microwave marine remote sensing, data fusion, image processing, and satellite oceanography.

Xiaofeng Li (M'00–SM'11) received the B.S. degree in optical engineering from Zhejiang University, Hangzhou, China, in 1985, the M.S. degree in physical oceanography from the First Institute of Oceanography, State Oceanic Administration, Qingdao, China, in 1992, and the Ph.D. degree in physical oceanography from North Carolina State University, Raleigh, NC, USA, in 1997.

During the M.S. Program, he completed the graduate course work with the Department of Physics, University of Science and Technology of China, Hefei, China. Since 1997, he has been with the National Environmental Satellite, Data, and Information Service (NESDIS), National Ocean and Atmospheric Administration (NOAA), College Park, MD, USA, where he is involved in developing many operational satellite ocean remote sensing products. He has authored more than 100 peer-reviewed publications and edited 4 books. His research interests include remote sensing oceanography and marine meteorology, satellite image processing, oil spill and coastal zone classification with multipolarization synthetic aperture radar (SAR), and the development of sea surface temperature algorithms.

Dr. Li received the Individual Award for Science from the NOAA/NESDIS Center for Satellite Applications and Research, the Outstanding Science and Research Employee of the Year Award from the U.S. Department of Commerce, the Len Curtis Award from the Remote Sensing and Photogrammetry Society, and the Overseas Expert Title from the Chinese Academy of Sciences. He is an Associate Editor of the IEEE TRANSACTIONS ON GEOSCIENCE AND REMOTE SENSING and the *International Journal of Remote Sensing*, the Ocean Section Editor-in-Chief of *Remote Sensing*, and an Editorial Board Member of the *International Journal of Digital Earth and Big Earth Data*.

Gang Zheng (SM'18) received the B.Eng. degree in electronic information engineering from Zhejiang University, Hangzhou, China, in 2003, and the M.S. and Ph.D. degrees in radio physics from the University of Electronic Science and Technology of China, Chengdu, China, in 2006 and 2010, respectively.

From 2010 to 2013, he was an Assistant Researcher with the State Key Laboratory of Satellite Ocean Environment Dynamics, Second Institute of Oceanography, Ministry of Natural Resources, Hangzhou, where he has been an Associate Researcher since 2013. His research interests include ocean microwave remote sensing, image processing, and electromagnetic numerical modeling.

Dr. Zheng served as the Guest Editor of *Remote Sensing* special issues on *AI-Based Remote Sensing Oceanography*, *Synergy of Remote Sensing and Modelling Techniques for Ocean Studies*, and *Tropical Cyclones Remote Sensing and Data Assimilation* from 2018 to 2019.